frontiers in Molecular Neuroscience

ORIGINAL RESEARCH
published: 09 April 2019
doi: 10.3389/fnmol.2019.00084

Direct Binding of the Flexible C-Terminal Segment of Periaxin to β4 Integrin Suggests a Molecular Basis for CMT4F

Arne Raasakka[1], Helen Linxweiler[1], Peter J. Brophy[2], Diane L. Sherman[2] and Petri Kursula[1,3]**

[1]Department of Biomedicine, University of Bergen, Bergen, Norway, [2]Centre for Discovery Brain Sciences, University of Edinburgh, Edinburgh, United Kingdom, [3]Faculty of Biochemistry and Molecular Medicine, University of Oulu, Oulu, Finland

The process of myelination in the nervous system requires a coordinated formation of both transient and stable supramolecular complexes. Myelin-specific proteins play key roles in these assemblies, which may link membranes to each other or connect the myelinating cell cytoskeleton to the extracellular matrix. The myelin protein periaxin is known to play an important role in linking the Schwann cell cytoskeleton to the basal lamina through membrane receptors, such as the dystroglycan complex. Mutations that truncate periaxin from the C terminus cause demyelinating peripheral neuropathy, Charcot-Marie-Tooth (CMT) disease type 4F, indicating a function for the periaxin C-terminal region in myelination. We identified the cytoplasmic domain of β4 integrin as a specific high-affinity binding partner for periaxin. The C-terminal region of periaxin remains unfolded and flexible when bound to the third fibronectin type III domain of β4 integrin. Our data suggest that periaxin is able to link the Schwann cell cytoplasm to the basal lamina through a two-pronged interaction *via* different membrane protein complexes, which bind close to the N and C terminus of this elongated, flexible molecule.

Keywords: myelin, Charcot-Marie-Tooth disease, periaxin, integrin, protein structural & functional analysis

OPEN ACCESS

Edited by:
Robert W. Burgess,
Jackson Laboratory, United States

Reviewed by:
Manzoor A. Bhat,
The University of Texas Health Science Center at San Antonio, United States
Julia Margaret Edgar,
University of Glasgow, United Kingdom

****Correspondence:***
Diane L. Sherman
diane.sherman@ed.ac.uk
Petri Kursula
petri.kursula@uib.no

Received: *23 January 2019*
Accepted: *19 March 2019*
Published: *09 April 2019*

Citation:
Raasakka A, Linxweiler H, Brophy PJ, Sherman DL and Kursula P (2019) Direct Binding of the Flexible C-Terminal Segment of Periaxin to β4 Integrin Suggests a Molecular Basis for CMT4F. Front. Mol. Neurosci. 12:84. doi: 10.3389/fnmol.2019.00084

INTRODUCTION

Long axonal segments in the vertebrate peripheral nervous system (PNS) are ensheathed by myelin, which accelerates nerve impulse propagation and supports axons both mechanically and trophically (Nave, 2010). A Schwann cell wraps its plasma membrane, partially excluding its cytosol, several times around a selected axonal process. This results in compact myelin, which has high lipid and protein content and is responsible for axonal insulation. Compact myelin is surrounded by a narrow compartment with higher cytosolic content, non-compact myelin, which acts as a supportive metabolic compartment to ensure long-term myelin stability (Hartline, 2008). Both myelin compartments contain a specific selection of proteins that have distinct tasks in ensuring the correct formation and stability of myelin; failure may result in one of several disease states, including the peripheral inherited neuropathies Charcot-Marie-Tooth (CMT) disease and Dejerine-Sottas syndrome (DSS). A large number of mutations in different PNS proteins has been linked to these conditions (Boerkoel et al., 2002; DiVincenzo et al., 2014). However, only a handful of CMT mutations have been characterized at the molecular structural level in order to understand the fine details of disease mechanisms (Sakakura et al., 2011; Mittendorf et al., 2014; Ruskamo et al., 2017).

The formation of myelin in the central nervous system (CNS) and PNS, as well as its lifelong maintenance, requires an intricate network of molecular interactions that link the myelin membrane, the cytoskeleton of the myelinating glial cell, and the extracellular matrix or the axonal surface together into a large supramolecular complex. A number of proteins, many of which seem specific for myelinating cells, have been pinpointed as playing roles in myelination; however, often the molecular details of the relevant processes and protein-protein interactions remain unknown. Myelin proteins have been specifically highlighted as a knowledge gap in structural biology in the past (Xie and Bourne, 2005), although more structural data from myelin proteins are becoming available. However, structures of protein-protein complexes of myelin-specific proteins mainly remain uncharacterized to date.

Unlike oligodendrocytic myelin in the CNS, Schwann cells in the PNS are surrounded by a carbohydrate-rich basal lamina, which is adhered to the outermost (abaxonal) Schwann cell plasma membrane bilayer *via* dystroglycans and α6β4 integrin, contributing to the mechanical stability of myelinated nerves (Einheber et al., 1993; Masaki et al., 2002; Nodari et al., 2008). Additionally, non-compact PNS myelin contains tight membrane-apposed structures at the abaxonal layer. These structures surround cytosolic channels of non-compact myelin, referred to as Cajal bands, which contain substantial microtubule-based transport as well as ribosomal activity (Ushiki and Ide, 1987; Sherman and Brophy, 2005). The membrane appositions have tight morphology and are enriched in periaxin (PRX)—the most abundant PNS non-compact myelin protein (de Monasterio-Schrader et al., 2012). Cajal bands and the membrane appositions are important in regulating myelin stability. These structures can be disturbed in human demyelinating diseases, as well as in corresponding mouse models (Sherman et al., 2001, 2012; Wu et al., 2012; Brennan et al., 2015). Furthermore, PRX influences the myelin sheath internode distance and thus influences nerve conduction velocity (Court et al., 2004; Wu et al., 2012).

Two isoforms of PRX are generated through alternative splicing (Dytrych et al., 1998). Disease mutations in PRX often truncate the long C-terminal region of the larger L-PRX isoform (Takashima et al., 2002). The molecular mechanism of disease in these cases has remained enigmatic, as the best-characterized protein interactions and functions of L-PRX so far lie very close to the N terminus. These include the PDZ-like domain, which mediates homo- and heterodimerization of PRX (Sherman et al., 2001; Han and Kursula, 2014; Yang and Shi, 2015), and the segment after it, which is known to bind dystrophin-related protein 2 (DRP2) and link PRX to the dystroglycan complex (Sherman et al., 2001). A conceivable additional mechanism of PRX function and role in disease could involve specific protein interaction sites at the C-terminal, isoform-specific end of L-PRX.

We wanted to identify novel binding partners for the L-PRX C-terminal region. The third cytoplasmic fibronectin-type III (FNIII) domain of β4 integrin (β4-FNIII-3) was identified as a high-affinity binder, and the complex was characterized using biophysical and structural biology techniques. The observed direct molecular interaction is likely to be important for the function of PRX and β4 integrin in developing mature myelin, and it provides a molecular basis for PRX mutations in CMT that result in the expression of truncated L-PRX.

MATERIALS AND METHODS

Yeast Two-Hybrid Screening

Yeast two-hybrid screening was performed essentially as previously described (Sherman et al., 2001). Briefly, a random-primed rat sciatic nerve cDNA library in λACTII was screened using the C-terminal region of rat L-PRX (residues 681–1383) in the pAS2-1 vector (Clontech) as bait. Three independent clones of β4 integrin each containing the third FNIII domain were found. To identify the domain of PRX, which interacted with β4 integrin, deletion constructs of PRX were made by PCR and subcloned into pAS2-1. β-galactosidase activity was tested by filter lift assays with one of the β4 integrin clones (62BpACTII).

GST Pulldown

The β4 integrin FNIII-3 domain (amino acids 1512–1593) cDNA was amplified by PCR and subcloned into pGEXKG. As a control, the adjacent fourth FNIII domain was cloned into the same vector. The recombinant protein was expressed and purified using a Glutathione-Sepharose 4B column as described (Sherman et al., 2001). GST pulldowns were performed by incubation of the GST fusion protein bound to Glutathione-Sepharose with a sciatic nerve lysate, as previously described by Sherman et al. (2001).

Immunoaffinity Chromatography

Immunoaffinity pulldowns were performed essentially as described (Sherman et al., 2001). PRX and β4 integrin in the pulldown fractions were identified by Western blot. PRX antibodies have been described (Sherman and Brophy, 2018). Antibodies against β4 integrin were raised in rabbits using a peptide corresponding to amino acids 1756–1772, to which an N-terminal cysteine was attached for coupling to keyhole limpet hemocyanin (CTEPFLIDGLTLGTQRLE), as described by Dytrych et al. (1998).

Immunofluorescence

Mice were perfused intravascularly with 4% paraformaldehyde in 0.1 M sodium phosphate buffer (pH 7.3), and sciatic nerve cryosections were prepared and immunostained as described by Gillespie et al. (2000). Antibodies against PRX have been described (Gillespie et al., 1994), and the monoclonal antibody against β4 integrin was a generous gift from Dr. S.J. Kennel, Biology Division, Oak Ridge National Laboratory.

Transfection and Coimmunoprecipitation

Full-length cDNA clones encoding rat β4 integrin and human α6 integrin were subcloned into the expression vectors pcDNA3.1 and pRC/CMV, respectively, and were generous gifts from Dr M.L. Feltri, Hunter James Kelly Research Institute, University of Buffalo and Dr Arnoud Sonnenberg, Netherlands Cancer Institute. PRX cDNA in the expression vector pCB6 has been described (Sherman and Brophy, 2000). PRX, β4 integrin,

and α6 integrin were expressed in HEK293 cells. After transfection, the proteins were immunoprecipitated as described by Sherman et al. (2001).

Proteomics

Proteomics analyses were carried out exactly as described by Sherman and Brophy (2018), comparing the PRX-bound proteomes of $PRX^{-/-}$ mice carrying a transgene for either wild-type PRX (PrxTg/$PRX^{-/-}$) or PRX with a C-terminal truncation mutation (mouse L-PRX truncated at residue 1016; ΔCPrxTg/$PRX^{-/-}$) corresponding to human CMT4F R1070X (Parman et al., 2004; Otagiri et al., 2006). Proteins from mouse nerve lysates were crosslinked followed by immunoprecipitation (IP) with a PRX antibody and then subjected to mass spectrometry (MS) analyses. Normalized abundance of β4 integrin was determined by MS using Progenesis (Nonlinear Dynamics) as described by Sherman and Brophy (2018).

Recombinant Protein Production

Synthetic genes encoding the rat L-PRX C-terminal region (UniProt ID: Q63425, amino acids 1036–1383; PRX-C) and rat β4-FNIII-3 (UniProt ID: Q64632, amino acids 1512–1602) were ordered from DNA2.0 (Newark, CA, USA) in the pJ401 bacterial expression vector. An additional sequence encoding an N-terminal hexahistidine tag, a short linker, and a tobacco etch virus (TEV) protease digestion site (MHHHHHHSSGVDLGTENLYFQS) was included at the start of the protein-coding insert.

PRX-C was expressed in *E. coli* BL21(DE3) using 0.4 mM IPTG induction for 1.5 h in LB medium containing 100 μg/ml ampicillin, at 37°C. After expression, the cells were pelleted by centrifugation and sonicated in Ni-NTA washing buffer (40 mM HEPES, 400 mM NaCl, 6 M urea, 20 mM imidazole, 1 mM PMSF, pH 7.5) supplemented with protease inhibitors (Roche). Purification was performed using Ni-NTA affinity chromatography and standard procedures. Elution was done with 32 mM HEPES, 320 mM NaCl, 4.8 M urea, 500 mM imidazole, pH 7.5. The eluted fraction was dialyzed at 4°C with constant stirring against 40 mM HEPES, 400 mM NaCl, 1 mM DTT, pH 7.5, before addition of recombinant TEV protease for affinity tag removal (van den Berg et al., 2006). The digestion was allowed to proceed overnight while dialyzing, which resulted in cleaved PRX-C with an additional N-terminal Ser residue. The protein was subjected to a second Ni-NTA step, in the absence of urea. The unbound and wash fractions were combined and concentrated, and sequential size exclusion chromatography (SEC) on a HiLoad Superdex 200 pg 16/600 column (GE Healthcare, Chicago, IL, USA) was used to separate the cleaved protein from contaminants and degradation products. Depending on downstream application, either 20 mM HEPES, 300 mM NaCl, 1% (v/v) glycerol, 0.5 mM TCEP, pH 7.5 (SEC buffer) or 20 mM HEPES, 150 mM NaCl, pH 7.5 (HBS) was used as running buffer.

β4-FNIII-3 was expressed in *E. coli* BL21(DE3) in LB or TB medium containing 100 μg/ml ampicillin, with 0.4 mM IPTG induction for 3 h at 37°C. The cells were harvested as above and resuspended in 40 mM HEPES, 400 mM NaCl, 20 mM imidazole, pH 7.5. After lysis by sonication, a Ni-NTA chromatography was carried out essentially as described above, omitting urea in all buffers. After Ni-NTA, the eluted protein was directly subjected to SEC using a HiLoad Superdex 75 pg 16/60 column (GE Healthcare, Chicago, IL, USA) using either HBS or SEC buffer.

Pulldown Experiment With Purified Proteins

Purified recombinant β4-FNIII-3 and PRX-C were used in pulldown experiments to confirm the direct interaction. PRX-C with and without the His-tagged β4-FNIII-3 was mixed with Ni-NTA agarose for 1 h at +4°C, in binding buffer (20 mM HEPES, 150 mM NaCl, 20 mM imidazole, pH 7.5). The matrix was collected by centrifugation at 150 *g* for 5 min at +4°C. Three washes with binding buffer were carried out, and proteins were eluted with 20 mM HEPES, 150 mM NaCl, 500 mM imidazole, pH 7.5. All fractions were analyzed with SDS-PAGE.

In addition, a partially degraded PRX-C sample was employed to identify fragments that do and do not bind β4-FNIII-3. The pulldown experiment was carried out exactly as above. Bands were excised from the gel and processed for tryptic peptide mapping.

Synchrotron Radiation Circular Dichroism (SRCD) Spectroscopy

SRCD data were collected from 0.15 to 0.6 mg/ml protein samples in 20 mM Na-phosphate, 150 mM NaF, pH 7.5 on the AU-CD beamline at the ASTRID2 synchrotron (ISA, Aarhus, Denmark). Closed circular cells with a pathlength of 100 μm (Suprasil, Hellma Analytics) were used for the measurements. Spectra were recorded from 170 to 280 nm at 20°C. Temperature scans were performed from 10 to 90°C in 5°C intervals, with 5 min incubation per time point, prior to spectral acquisition.

Buffer spectra were subtracted from the protein samples, and CD units were converted to $\Delta\varepsilon$ (M^{-1} cm^{-1}), using rPRX-C concentration determined using refractometry and/or rFNIII-3 concentration determined using absorbance at 280 nm. Deconvolution was performed using DichroWeb (Whitmore and Wallace, 2004) with the CDSSTR algorithm (Johnson, 1999) and SP175 reference set (Lees et al., 2006) or using BeStSel (Micsonai et al., 2018). Secondary structure prediction was performed using JPred (Drozdetskiy et al., 2015).

Small-Angle X-Ray Scattering (SAXS)

Synchrotron SEC-SAXS data for PRX-C, β4-FNIII-3, and their complex were collected on the B21 beamline at Diamond Light Source (Didcot, UK) using an online size exclusion setup. The chromatography was performed using an Agilent 1200-series HPLC system and a Superdex 200 increase 3.2/300GL (GE Healthcare, Chicago, IL, USA) column with 20 mM Tris-HCl, 150 mM NaCl, pH 7.4 as mobile phase at an isocratic flow of 0.04 ml/min. Injections (45 μl) of 6.5–9.8 mg/ml total protein were performed for PRX-C, β4-FNIII-3, and their equimolar complex (145 μM each). Scattering was directly

recorded from the eluted proteins at 6 s exposure per frame, 591 frames per run. The frames containing a stable R_g within an eluted I_0 peak were selected and combined using ScÅtter[1]. Data were processed and analyzed using the ATSAS package (Petoukhov et al., 2012). GNOM was used to calculate distance distribution functions (Svergun, 1992), and *ab initio* modeling was performed using GASBOR (Svergun et al., 2001). Multiphase modeling of protein complex data was performed using MONSA (Svergun, 1999) rigid body refinement with SASREF (Petoukhov and Svergun, 2005), and ensemble optimization analysis with EOM (Bernadó et al., 2007); see **Supplementary Table S1** for further details.

For intrinsically disordered proteins (IDPs), more accurate values of R_g can be obtained from SAXS data using the Debye formalism. Briefly, by plotting $[I(s)]^{-1}$ vs. $s^{2.206}$, in the range $(s\ R_g)^2 < 3$, one can use much more data than in a regular Guinier plot. Here, a linear fit of the plot is used to obtain $R_g = (a/0.359b)^{0.453}$; a = slope, b = y intercept (Calmettes et al., 1994). Theoretical values for R_g and D_{max} for a random chain can be calculated from sequence length as follows: $R_g = R_0N^{\nu}$; $R_0 = 1.98$ Å, N = number of residues, $\nu = 0.602$ (Fitzkee and Rose, 2004) for denatured proteins; $R_0 = 2.54$ Å, $\nu = 0.522$ (Bernadó and Blackledge, 2009) for IDPs. Average end-to-end distance can be estimated as $<L^2> = L_0N$; $L_0 = 81.8$ Å (Fitzkee and Rose, 2004).

Mass Spectrometry and Covalent Crosslinking

The molecular weight of PRX-C and β4-FNIII-3 was verified by MS. In short, the undigested masses were determined with ultra-performance liquid chromatography (UPLC)-coupled electrospray ionization (ESI) time-of-flight MS in positive ion mode, using a Waters Acquity UPLC-coupled Synapt G2 mass analyzer with a Z-Spray ESI source.

Protein crosslinking was carried out to conjugate surface-exposed carboxylate sidechains with lysines with a zero-length crosslinker. All crosslinking reactions were carried out at 40 μM final protein concentration in 100 mM bis-tris methane, 150 mM NaCl, 4 mM 1-ethyl-3-(3-dimethylaminopropyl)carbodiimide, 20 mM *N*-hydroxysuccinimide, pH 6.5. The activation step was allowed to proceed for 15 min at ambient temperature, followed by quenching the reactions through adding 2-mercaptoethanol to 20 mM. After addition of the second protein in selected reactions, incubation was continued for another 3 h at ambient temperature and stopped by adding ethanolamine to 10 mM. The reactions were analyzed using SDS-PAGE.

The crosslinked proteins were identified using matrix-assisted laser desorption/ionization time-of-flight (MALDI-TOF) MS. From stained SDS-PAGE gels, gel bands were cut, staining removed by sequential washing with 50 mM NH_4HCO_3 in 40% acetonitrile (ACN). Proteins were subjected to in-gel Cys reduction using 20 mM DTT and subsequent alkylation using 40 mM α-iodoacetamide. After this, all proteins were in-gel digested [20 ng of trypsin (Sigma-Aldrich) per gel piece], followed by peptide extraction from gel pieces using 30% ACN/0.1% trifluoroacetic acid (TFA), and transfer to a Bruker anchor plate. 800 μg/ml α-cyano-4-hydroxy cinnamic acid in 85% ACN/0.1% TFA with 1 mM $NH_4H_2PO_4$ was used as matrix. Peptide mass spectra and MS/MS spectra were measured with a Bruker Ultra fleXtreme MALDI-TOF mass spectrometer and compared to theoretical spectra generated using the known protein sequences.

Multi-Angle Static and Quasielastic Light Scattering

SEC-MALS and quasielastic light scattering (QELS) data were collected to determine the monodispersity, hydrodynamic radius, and molecular weight of PRX-C, β4-FNIII-3, and their equimolar complex (145 μM each). The chromatography was performed using an Agilent 1200-series HPLC system and a Superdex 200 increase 3.2/300GL (GE Healthcare, Chicago, IL, USA) column with 20 mM Tris, 150 mM NaCl, pH 7.4 as a mobile phase. Protein samples of 160–250 μg were injected into the column at an isocratic flow of 0.04 ml/min, and light scattering was recorded using a Wyatt miniDAWN HELEOS-II instrument with 18 detectors and a QELS module at ambient temperature. The refractive index was measured using a Wyatt Optilab T-rEX refractometer and used as the concentration source. All data were analyzed using the ASTRA software (Wyatt).

Protein Crystallography

β4-FNIII-3 was crystallized using sitting-drop vapor diffusion in drops consisting of 150 nl protein solution (12.7 mg/ml in SEC buffer) mixed with 150 nl of reservoir solution. Initially, crystals were formed in a wide variety of PEG-based conditions in PACT Premier and JCSG+ (Molecular Dimensions) crystal screens. Optimized crystals used for diffraction data collection were grown at 20°C in conditions containing 16%–22% (w/v) PEG 3350 and 180–240 mM NH_4NO_3.

Prior to diffraction data collection, the crystals were cryoprotected briefly by adding 1.5 μl of cryoprotectant solution directly into the sitting drop mix. The cryoprotectant consisted of 75% (v/v) well reservoir and 25% (v/v) PEG 400. After soaking in cryoprotectant, crystals were mounted in loops and snap-frozen in liquid N_2.

X-ray diffraction data were collected at 100 K on the P13 beamline, EMBL/DESY, Hamburg, Germany (Cianci et al., 2017) and the ID30A-1 beamline at ESRF (Grenoble, France; Bowler et al., 2015; Svensson et al., 2015). Data were processed using XDS (Kabsch, 2010). Phasing was performed with molecular replacement using the human β4-FNIII-3 structure (PDB ID 4wtw; Alonso-García et al., 2015) as the search model in Phaser (McCoy et al., 2007). The structure was refined in phenix.refine (Afonine et al., 2012), and model building was done in Coot (Emsley et al., 2010). The low solvent content of 36% (including ordered water) leads to a higher-than-average difference between R_{work} and R_{free} during structure refinement.

The structure was validated and analyzed using DSSP (Kabsch and Sander, 1983), MolProbity (Davis et al., 2004), PyMOL, PDB2PQR (Dolinsky et al., 2004), APBS (Jurrus et al., 2018), and UCSF Chimera (Pettersen et al., 2004). The crystal structure was

[1]http://www.bioisis.net/tutorial

subjected to atomistic molecular dynamics simulations for 550 ns in YASARA (Krieger and Vriend, 2015), essentially as described by Ponna et al. (2017).

Isothermal Titration Calorimetry (ITC)

PRX-C and β4-FNIII-3 were dialyzed into HBS overnight to ensure matching buffer. The proteins were passed through a 0.22-μm filter, and concentrations were checked. Isothermal titration calorimetry (ITC) was performed at 25°C using a Malvern MicroCal iTC200 calorimeter with reference power set to 5 μcal/s. 680 μM β4-FNIII-3 was titrated into 350 μl of 68 μM PRX-C under constant stirring. A total of 38 1-μl injections were performed, with a 240-s waiting period between injections. Data were analyzed using Origin. The titration experiment was repeated twice with two separate protein batches and nearly identical values were obtained in each case.

Four different peptides from PRX-C predicted to represent a putative binding site were ordered from Genscript with N-terminal acetylation and C-terminal amidation, and they were similarly used to follow binding to β4-FNIII-3 with ITC. The experiment was done at 25°C with 2-μl injections with 150-s intervals. The cell contained 100 μM His-β4-FNIII-3 and the syringe 1 mM peptide. The peptide sequences were ASFGEAGPEIAAPSAEGTVG (peptide 1; residues 1091–1110), RIQVPQVMLELPGTQVAGGDLL (peptide 2; residues 1112–1133), GEGIFKMPTVTVPQLELDVGLGHEAQ (peptide 3, residues 1135–1160), and SGRRGRVRVRLPRVGLASPSK (peptide 4; residues 1290–1310).

Thermal Stability Assays

Thermal stability experiments were performed for 0.25–2 mg/ml β4-FNIII-3 and a 20 μM equimolar complex of PRX-C and β4-FNIII-3 in SEC buffer using a label-free fluorescence-based approach (nanoDSF). The instrument used was a NanoTemper Prometheus NT.48 nanoDSF with a backscattering option to detect aggregation onset. Each 10-μl sample was loaded inside a glass capillary, and a constantly monitored scan from 20 to 95°C using a 2°C/min ramp rate was performed. Fluorescence at emission wavelengths 330 nm and 350 nm (F_{330} and F_{350}, respectively) was monitored, and a single transition event was observed in the fluorescence ratio (F_{350}/F_{330}) in all samples. Melting temperature midpoint (T_m) values were extracted from the first derivative peak maximum.

RESULTS

Identification of the Cytoplasmic Domain of β4 Integrin as a Potential Periaxin Ligand

In order to identify putative protein ligands for the C-terminal segment of L-PRX, which is missing in the presence of the CMT4F R1070X mutation (Otagiri et al., 2006; Sherman and Brophy, 2018), we carried out a yeast 2-hybrid screen of a rat sciatic nerve cDNA library with the C-terminal segment, missing upon the R1070X mutation, as bait. As a result, we obtained three separate clones containing the β4-FNIII-3 domain (**Figure 1A**). One of these (clone 62B) was further used in confirmatory experiments.

The interaction was confirmed and the binding site coarsely mapped by using different domains of L-PRX in the screen, with the obtained β4 integrin construct 62B as bait (**Figure 1B**). The results indicate that the last ∼350 residues, containing the acidic region of L-PRX, are crucial for the interaction in this system. Interestingly, both PRX(996–1165) and PRX(1168–1383) gave negative results, suggesting that the binding site may be located close to the point separating these two constructs, or that the site might be a combination of more than one PRX segment required to come together for high-affinity binding.

Evidence for β4 Integrin-PRX Interaction in Tissues and Cells

As the next step, GST pulldowns from sciatic nerve lysates were carried out using a GST-β4-FNIII-3 construct. Western blotting identified L-PRX in the fraction bound to the GST fusion protein, but not GST alone (**Figure 1C**). DRP2 was also identified in the fraction pulled down by GST-β4-FNIII-3, while GST-β4-FNIII-4 was unable to pull down PRX or DRP2 (**Supplementary Figure S1**). Immunoaffinity pulldowns were further carried out using an anti-PRX antibody, and an analysis of the fractions showed copurification of L-PRX and β4 integrin (**Figure 1D**) when SDS—breaking up protein complexes—was not used during extraction.

The putative interaction between L-PRX and β4 integrin was further studied using co-IP from cultured HEK293 cells overexpressing both proteins. After IP with either β4 integrin or PRX antibodies, both proteins were observed in the eluted fraction, showing they are present in the same complex (**Figure 1E**).

To observe the localization of PRX and β4 integrin in myelinating glial cells, immunofluorescence staining of mouse sciatic nerves was carried out. The result confirms earlier studies (Einheber et al., 1993; Feltri et al., 1994; Scherer et al., 1995), in that both PRX and β4 integrin are localized at the outermost membrane layer of myelin (**Figure 1F**).

Changes in the L-PRX Interactome in a Mouse Model of CMT4F

The mouse model for CMT4F (Sherman and Brophy, 2018), ΔCPrxTg/Prx$^{-/-}$, carries a truncating mutation mimicking human L-PRX with the R1070X mutation. The phenotype of this mouse mutant involves the loss of abaxonal membrane appositions and shortening of internodal lengths (Sherman and Brophy, 2018), while the Prx$^{-/-}$ phenotype presents initial hypermyelination with progressing demyelination and neuropathic pain behavior; for a full description, see Gillespie et al. (2000). We carried out proteomics experiments to follow the expression level of possible PRX ligand proteins in the ΔCPrxTg/Prx$^{-/-}$ model. PRX was immunoprecipitated from mouse nerves after crosslinking, and the bound proteins were analyzed and compared between the ΔCPrxTg/Prx$^{-/-}$ and PrxTg/Prx$^{-/-}$ samples. The levels of DRP2 were decreased in the PRX interactome of ΔCPrxTg/Prx$^{-/-}$ mutant animals (Sherman and Brophy, 2018). In addition, a several-fold drop in the level of β4 integrin could here be observed in the mutant compared to the PrxTg/Prx$^{-/-}$ animals based on data from the same experiment

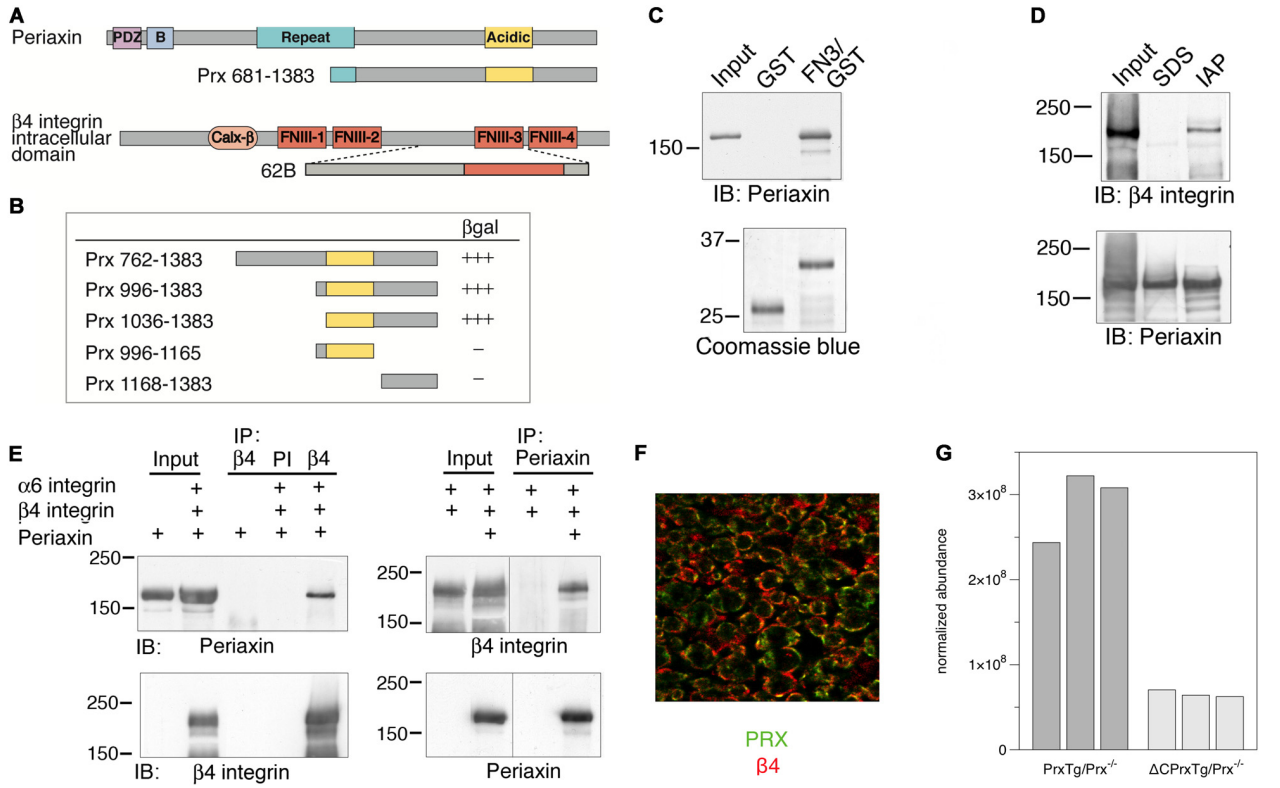

FIGURE 1 | Identification of an interaction between periaxin and β4 integrin. **(A)** Top: structure of full-length L-PRX and the bait used in a yeast two-hybrid screen using the C terminus of L-PRX (aa 681–1383) fused to the GAL4 DNA-binding domain. Bottom: structure of the intracellular domain of β4 integrin and one (62B) of the three clones recovered from the screen, all of which included the third FNIII domain of β4 integrin. **(B)** Identification of the region of PRX, which binds to β4 integrin. The strength of interaction between the 62B clone and a series of PRX constructs in a yeast two-hybrid β-galactosidase assay was assessed semiquantitatively by the time taken for colonies to turn blue (+++, 30 min; ++, 30–60 min; +, 60–180 min). **(C)** Interaction of β4-FNIII-3 with PRX *in vitro*. GST or a GST-β4-FNIII-3 fusion protein were incubated with a sciatic nerve lysate *in vitro* and any bound L-PRX was detected by Western blotting (IB) using a PRX antibody after SDS-PAGE. The input lane confirms the presence of PRX in the lysate. Coomassie blue staining shows that equivalent amounts of GST and the GST fusion proteins were used. **(D)** Immunoaffinity copurification of β4 integrin and PRX. Detergent extracts of mouse sciatic nerve in the non-ionic detergent Igepal were incubated with beads, to which affinity-purified sheep anti-PRX antibodies had been covalently coupled. After extensive washing, bound proteins were eluted and analyzed by SDS-PAGE and Western blotting. The SDS control lane contains proteins that bound to the beads after first solubilizing the nerves in SDS to disrupt protein-protein interactions, followed by dilution of the SDS with Triton X-100. **(E)** Coimmunoprecipitation of β4 integrin and PRX from transfected HEK293 cells. PRX and β4 integrin were detected by Western blot (IB) after immunoprecipitation (IP) with β4 integrin antibodies when β4 integrin, α6 integrin, and PRX were coexpressed. Preimmune serum (PI) did not precipitate either protein. Reciprocally, β4 integrin and PRX were detected by Western blot after IP with anti-PRX antibodies, when β4 integrin, α6 integrin, and PRX were coexpressed. **(F)** Immunohistochemistry. Both PRX (green) and β4 integrin (red) localize at the abaxonal membrane in mature myelin. **(G)** Quantification of β4 integrin from the IP of crosslinked sciatic nerves from the full-length PRX transgenic mouse on a PRX null background (n = 3) vs. C-terminally truncated PRX transgene on a PRX null background (n = 3).

(**Figure 1G**). The result provides strong evidence for a functional protein complex involving L-PRX and β4 integrin in mouse peripheral nerve myelin *in vivo*.

Complex of Purified Recombinant β4 Integrin and PRX

The above experiments provided evidence for a direct interaction between L-PRX and β4 integrin in myelinating Schwann cells. We conducted a biophysical characterization of the interaction using recombinant PRX-C and β4-FNIII-3.

Pulldown experiments with the purified components confirmed the direct molecular interaction suggested by the data above. His-tagged β4-FNIII-3 pulled down PRX-C (**Figure 2A**). Pulldown of a partially degraded PRX-C sample showed that essentially all PRX fragments on the SDS-PAGE gel were pulled down by β4-FNIII-3 (**Figure 2B**). MS analysis indicated that the shortest fragments were missing the very C-terminal regions, while the acidic domain was well-covered in all fragments (data not shown), suggesting that the N-terminal half of the PRX-C construct contained the binding site.

SEC-MALS and QELS experiments verified the interaction *in vitro*, whereby the observed complex mass fit to a 1-to-1 complex, with an increased hydrodynamic radius (R_h) compared to the individual interaction partners alone (**Figure 2C**, **Table 1**). R_h of the complex was only slightly higher than that for PRX-C, indicating that the complex remained in an extended overall conformation; this is also reflected in the very small change in SEC elution volume. As β4-FNIII-3 is small

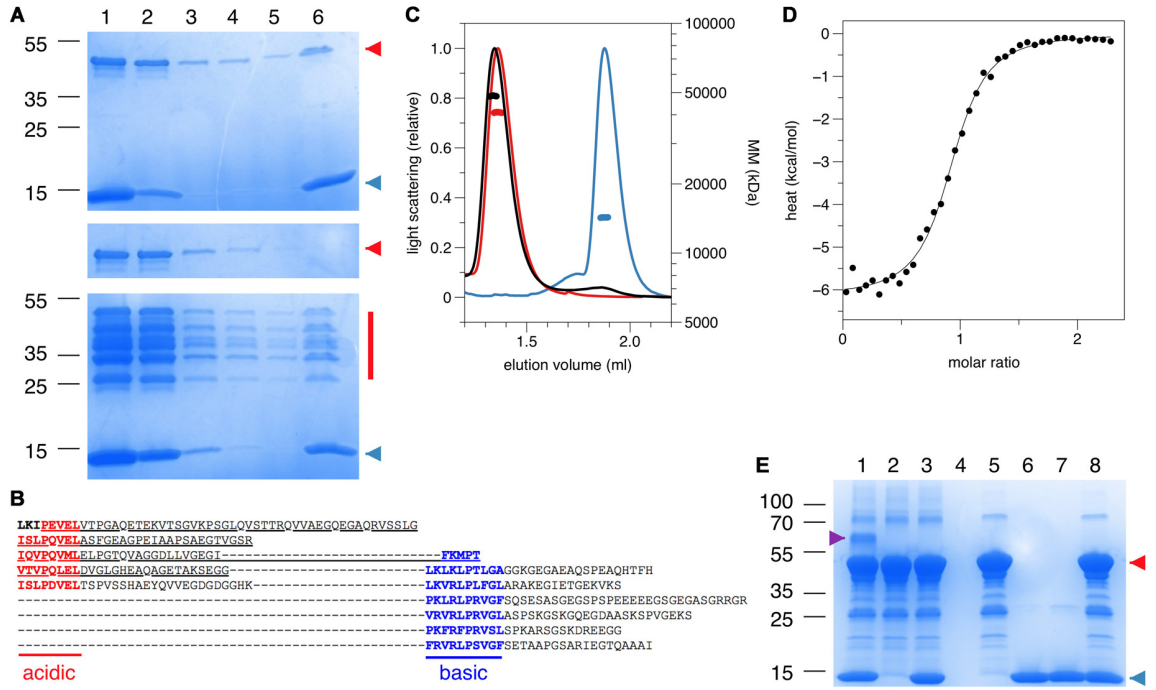

FIGURE 2 | Direct molecular interaction assays using purified recombinant proteins. **(A)** Pulldown with pure recombinant proteins on a Ni-NTA affinity matrix. Top, PRX-C and His-tagged β4-FNIII-3; middle, PRX-C alone; bottom; partially degraded PRX-C and His-tagged β4-FNIII-3. Samples: 1, input sample; 2, unbound fraction; 3–5, washes; 6, elution. PRX-C is indicated in red and β4-FNIII-3 in blue. Sizes of molecular weight markers are indicated on the left (kDa). **(B)** Sequence of the PRX-C construct, indicating the presence of acidic and basic repeats. The underlined segment (the acidic domain) can be detected in all the PRX-C bands in the bottom panel of **(A)**. **(C)** Size exclusion chromatography (SEC)-MALS analysis shows molecular mass expected for a 1:1 complex. PRX-C, red; β4-FNIII-3, blue; complex, black. **(D)** Isothermal titration calorimetry (ITC) titration of the complex indicates 1:1 stoichiometry. $\Delta H = 6.2 \pm 0.06$ kcal/mol, $\Delta S = 5.8$ cal/mol°. **(E)** Covalent crosslinking. The complex is only visible when both proteins have been activated (Lane 1). The magenta arrowhead indicates the 1:1 complex. PRX-C is indicated in red and β4-FNIII-3 in blue. Samples: 1, both proteins activated; 2, PRX-C activated; 3, PRX-C activated, β4-FNIII-3 added; 4, no activation; 5, no activation, PRX-C added; 6, no activation, β4-FNIII-3 added; 7, β4-FNIII-3 activated; 8, β4-FNIII-3 activated, PRX-C added.

and tightly folded, this implicates that the PRX-C segment does not become compact upon complex formation, which would be indicated by a decreased R_h.

A dissociation constant of 1.7 ± 0.1 μM was obtained for the protein-protein complex using ITC, with a binding stoichiometry of ∼1 (**Figure 2D**), being in good corroboration with the light scattering data above. Hence, the C-terminal region of L-PRX and β4-FNIII-3 bind each other with a low micromolar affinity, in a complex tight enough to survive e.g., separation by SEC. The stoichiometry suggests that the interaction site is either distinct from the repeat sequences in L-PRX, or that maximally one β4 integrin molecule can bind to PRX-C even if the binding site would involve the repeats. For more insight, ITC was repeated with selected peptides representing different features of the PRX-C sequence, but no binding to these linear peptide motifs was observed (**Supplementary Figure S2**).

Covalent crosslinking and MS were used in an attempt to map the binding site in more detail. An additional band containing both proteins was apparent on SDS-PAGE after crosslinking (**Figure 2E**). MS analysis of tryptic peptides from this band confirmed the presence of both PRX-C and β4-FNIII-3, but no conclusions could again be drawn on the exact binding site.

Thermal stability of the proteins was studied using label-free differential scanning fluorimetry (nanoDSF), whereby the signal came from the folded β4-FNIII-3 domain. β4-FNIII-3 has the same melting point (+70°C) in the presence and absence of PRX-C (**Table 2**), suggesting no large structural changes are induced by PRX-C binding.

Taken together, the above experiments have shown a direct protein-protein interaction between β4-FNIII-3 and PRX-C. However, the detailed binding mode and binding site(s) remain to be identified.

Structural Insights into the Protein-Protein Complex

While PRX-C is predicted to contain segments of β strand, the purified protein is essentially unfolded, as shown by SRCD spectroscopy (**Figure 3A**, **Table 2**). The β strand predictions coincide with repeats in the sequence (**Figure 3B**), and they could be of functional relevance in ligand protein binding and induction of secondary structures in PRX-C.

SRCD was used to shed light on possible changes in secondary structure content accompanying complex formation. The spectra clearly show that the overall secondary structure content remains identical in the complex, compared to the two proteins in

TABLE 1 | Characterization of the PRX-C/β4-FNIII-3 complex mass and size.

	MS	SEC-MALS			QELS	SEC-SAXS	
	M_r (measured), Da	M_r (measured), kDa	M_r (theoretical), kDa	% of expected	R_h(nm)	R_g(nm) Guinier/Debye/ Theoretical denatured, IDP/EOM	D_{max}(nm) GNOM/ Theoretical/EOM
PRX-C	35869	41.00 ± 0.02	35.87	114	4.79 ± 0.08	5.68 ± 0.04/6.21/6.75, 5.39/6.14	23.0/16.9/19.6
β4-FNIII-3	12756	14.30 ± 0.02	12.76	112	2.15 ± 0.04	2.11 ± 0.01/–/–/–	9.8/–/–
Complex	-	48.27 ± 0.04	48.63	99	5.22 ± 0.08	5.69 ± 0.06/6.11/–, –/–	25.2/–/–

isolation (**Figure 3A**). Together with the SAXS data (see below), SRCD shows that upon β4-FNIII-3 binding, the PRX C-terminal segment does not obtain large amounts of folded structure. Heat denaturation experiments by SRCD confirmed the same melting point for β4-FNIII-3 in the presence and absence of PRX-C (**Table 2**).

To aid in structural modeling and understanding the interactions in the complex, we solved the high-resolution crystal structure of the rat β4-FNIII-3 domain (**Figure 4**, **Table 3**). The structure is similar to the human β4-FNIII-3 domain (Alonso-García et al., 2015), consisting of a β sandwich made of seven β strands. In two of the four monomers in the asymmetric unit, the His tag could be partially seen in electron density, being in different conformations (**Figure 4**).

Purified PRX-C was subjected to SAXS experiments to gain more insight into its flexibility, molecular dimensions, and conformational ensembles. These experiments indicate that PRX-C behaves much like a random polymer chain and is highly extended (**Figure 5**, **Table 1**).

While SAXS indicated a highly disordered nature for PRX-C alone, we wanted to observe, whether it becomes more ordered in the complex with β4-FNIII-3. The β4-FNIII-3 crystal structure was used to model the solution structure of the complex, which cannot be crystallized due to the flexible nature of PRX and the fact that the exact binding site remains unknown. SAXS analysis of the protein complex, based on a SEC-SAXS experiment, shows that PRX-C remains elongated, and extra density corresponding to the size of a β4-FNIII-3 molecule appears close to one end of the complex (**Figures 5D,E**). This is in line with the results from SEC-MALS (see above).

The structure of β4-FNIII-3 can be used to predict the binding site for PRX. A surface analysis of the domain crystal structure indicates an elongated hydrophobic groove lined by β strands 4 and 5 (**Figures 4**, **6A**), which could accommodate a linear motif, possibly in a β conformation; this would extend the smaller β sheet from 3 to 4 β strands. MD simulations of the structure further show that this region is the most mobile segment of β4-FNIII-3, and the cavity can open even more (**Figures 6B–D**). Furthermore, although the FNIII-3 and -4 domains of β4 integrin are rather homologous, sequence conservation in the possible binding site is very low—in line with the observation that FNIII-4 does not bind to PRX (**Supplementary Figure S1**). More detailed structural data can be obtained, once the exact binding site(s) have been identified.

DISCUSSION

At the cellular level, myelin formation involves a substantial amount of lipid and protein synthesis and their subsequent assembly into a multilayered, tightly packed proteolipid multilayer. The molecular interactions involved in this process can be roughly divided into those involved in the formation of the compact myelin compartment, and into those relevant for non-compact myelin. This division does not imply that a single protein cannot take part in both aspects; for example, myelin basic protein functions both in membrane packing and in the regulation of cytoplasmic channels (Snaidero et al., 2017).

TABLE 2 | Folding and thermal stability of PRX-C and β4-FNIII-3.

	SRCD deconvolution*			Secondary structure prediction**			T_m, °C	
	% helix	% strand	% other	% helix	% strand	% other	SRCD	nanoDSF
PRX-C	3	38	58	0	7.7	92.3	-	-
	3	31	66					
β4-FNIII-3	1	45	51	0 (0)	37.2 (34.5)	62.8 (65.5)	59.5 ± 0.6	69.8 ± 0.1
	2	50	49					
Complex	2	39	56	0	14.9	85.1	58.8 ± 0.7	70.3 ± 0.1
	3	35	61					

**Deconvolved using DichroWeb (values above), or with BeStSel (values below). ** Predicted from primary structures using JPred. Values in brackets were extracted from the crystal structure using DSSP. The complex values were calculated from the JPred predictions, assuming a 1:1 complex.*

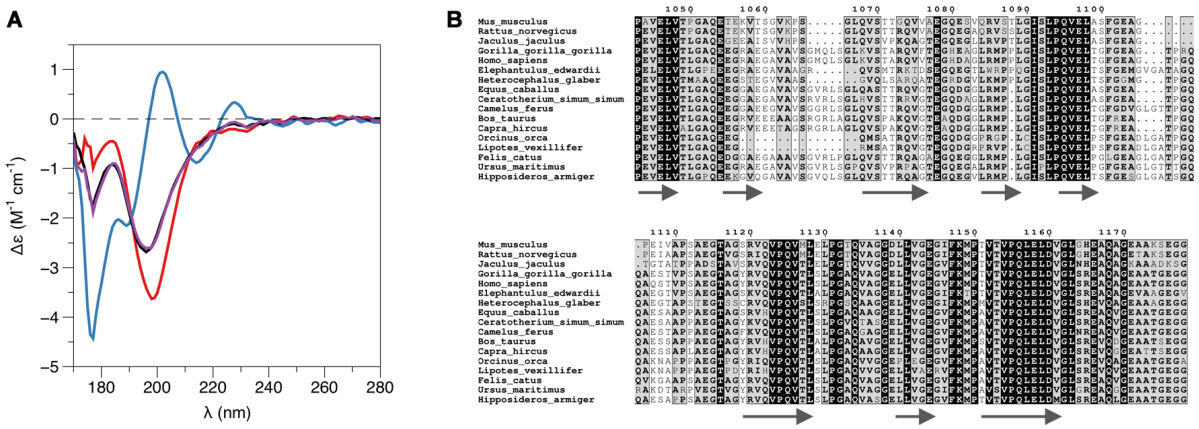

FIGURE 3 | L-PRX remains disordered in the complex. **(A)** Synchrotron radiation circular dichroism (SRCD) spectroscopy. PRX-C, red; β4-FNIII-3, blue; complex, black; sum of individual protein spectra, magenta. **(B)** Secondary structure predictions of the PRX-C acidic region, aligned from selected species.

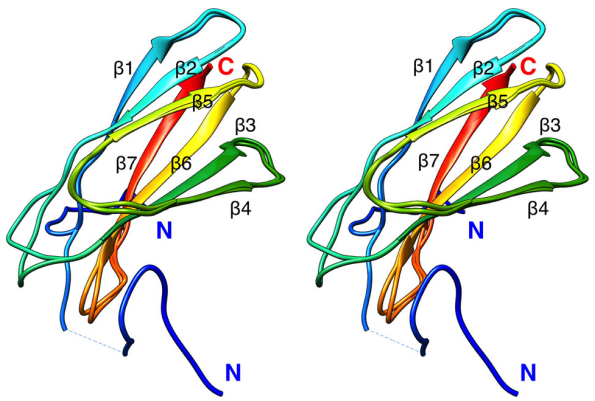

FIGURE 4 | Crystal structure of rat β4-FNIII-3 (stereo view). Two of the four individual chains in the asymmetric unit are shown. The chain is colored from the N (blue) to the C (red) terminus. The His-tag is partially resolved at the N terminus, and takes different conformations in different monomers. Secondary structure elements are labeled.

Both PRX and β4 integrin play important roles in peripheral nerve myelination (Gillespie et al., 2000; Court et al., 2004; Nodari et al., 2008). Recently, it was suggested that PRX may be a ligand for β4 integrin (Poitelon et al., 2018), and the interaction has been mentioned before (Wu et al., 2012), but not studied in detail. We set out to confirm this putative direct molecular interaction and to obtain 3D structural data on the protein-protein complex formed by PRX and β4 integrin.

L-PRX Binds β4 Integrin Directly With High Affinity

Integrins are involved in myelination by both oligodendrocytes (CNS) and Schwann cells (PNS). In Schwann cells, the two main isoforms of integrin are α6β1 and α6β4. While α6β1 is expressed in the early stages of myelination and is crucial for the radial sorting of axons (Feltri et al., 2002; Poitelon et al., 2016), α6β4 is predominant in the late stages and mature myelin (Einheber et al., 1993; Feltri et al., 1994). This indicates a developmental switch during myelination and suggests that β4 integrin is important for myelin maturation and maintenance. The levels of the Schwann cell laminin receptors integrin α6β1, α6β4 and dystroglycan are all regulated by the transcriptional co-activators Yap and Taz (Poitelon et al., 2016). The two basal lamina receptors of mature myelin, α6β4 integrin and dystroglycan, known to be together responsible for myelin stability (Nodari et al., 2008), are according to our results bound to the same scaffold protein, L-PRX, at the Schwann cell abaxonal plasma membrane.

We have shown here with a collection of methods that L-PRX binds, through its C-terminal region, directly to β4-

TABLE 3 | Crystallographic data collection and refinement statistics.

Data collection statistics	
Beamline	ID30A-1 (ESRF)
Space group	$P2_12_12_1$
Unit cell *a, b, c* (Å)	51.22, 52.84, 144.53
Wavelength (Å)	0.966
Resolution (Å)	50–1.60 (1.64–1.60)
Unique reflections	51757 (3746)
Multiplicity	3.3 (3.3)
Completeness (%)	98.3 (98.6)
R_{merge} (%)	6.1 (239.2)
R_{meas} (%)	7.3 (283.9)
$<I / \sigma(I)>$	8.8 (0.6)
$CC_{\frac{1}{2}}$ (%)	99.8 (16.6)
Wilson *B* ($Å^2$)	39.2
Refinement statistics	
R_{cryst} (%)	19.0
R_{free} (%)	23.9
RMSD bond length (Å)	0.013
RMSD bond angle (°)	1.1
Mean *B* value ($Å^2$)	49.7
Ramachandran plot	
Res. in favored regions (%)	95.9
Outlier residues (%)	0.8
MolProbity score/percentile	2.05/44th
PDB entry	6HYF

Values in parentheses correspond to the highest-resolution shell.

FNIII-3 with high affinity. Considering the presence of both proteins in a large protein scaffold at the Schwann cell outermost membrane, it is likely that the affinity is even higher when full-length proteins interact and avidity is increased by e.g., protein clustering and oligomerization. PRX could function as a ruler between integrins and dystroglycans on the cell surface; on the other hand, changes in the clustering of these molecules, e.g., through changes in the basal lamina, might affect the conformation of PRX as well as its cytosolic interactions. The importance of these interactions could lie in defining the boundaries of the appositions and Cajal bands at the abaxonal membrane, as DRP2 is restricted to the appositions and integrin signaling occurs at Cajal bands (Salzer, 2015). It is possible that PRX binds to DRP2 in appositions and β4 integrin at Cajal bands separately. Clearly, more detailed *in vivo* experiments will be required to resolve these important details.

The exact binding site of β4 integrin on L-PRX remains to be determined. Despite a number of approaches, we were not able to highlight a short segment responsible for binding. Despite the presence of two kinds of repeats in the PRX-C sequence, neither of these was enough to bind alone. Mapping of the binding site through the yeast two-hybrid experiments also proved to be inconclusive; while the full PRX-C region showed strong binding, cutting the region in two (constructs 996–1165 and 1168–1383) resulted in the loss of detectable interaction. It is likely that the binding to β4 integrin involves more than one segment of PRX-C—possibly a combination of an acidic and a basic repeat. This will clearly be a subject of more detailed structural studies in the future.

Similarly to the reduction seen here in the PRX interactome of β4 integrin in mice with truncated L-PRX, corresponding to human CMT4F mutation R1070X (Sherman and Brophy, 2018), a recent study (Poitelon et al., 2018) showed the loss of PRX from the β4 integrin interactome in mice with β4 integrin deficiency. It was thereby suggested that PRX might link β4 integrin functionally to PMP22 (Poitelon et al., 2018), but a direct or indirect interaction between PRX and PMP22 remains to be detected.

L-PRX Is Intrinsically Disordered

The C-terminal segment of L-PRX is highly flexible and intrinsically disordered, as shown by structure predictions, SRCD spectroscopy, and SAXS. The potential of intrinsically disordered regions in mediating specific protein interactions has been recently highlighted in number of studies (Barbar and Nyarko, 2015; Jie et al., 2015; Myllykoski et al., 2018). Such complexes involve usually the recognition of short linear motifs by a folded binding partner. In the current case, PRX-C remains highly flexible even upon β4 integrin binding. Considering the ratio R_g/R_h, the complex, having a lower ratio, is likely to be somewhat less flexible than PRX-C alone. Molecular flexibility may be important for the supramolecular organization of the protein scaffold at the outermost layer of PNS myelin, whereby PRX plays a central role.

Intriguingly, many of the myelin-specific proteins have a high degree of intrinsic disorder, as well as specific interactions, which makes myelin an interesting case for studying biomedically relevant intrinsically disordered proteins and their interactions. A well-studied example is the myelin basic protein, which is intrinsically disordered in solution, but partially folds upon membrane binding (Harauz et al., 2009; Raasakka et al., 2017). MOBP and the cytoplasmic domain of P0 are predicted to be disordered (Han et al., 2013), and the latter is intrinsically disordered in solution (Luo et al., 2007; Raasakka et al., 2019a). The cytoplasmic domain of the large myelin-associated glycoprotein is an intrinsically disordered protein but forms a specific heterotetramer upon dynein light chain binding, which is likely to help in dimerization and affect binding to the axonal surface (Myllykoski et al., 2018).

In addition to the C-terminal segment studied here, most of the L-PRX-specific region is predicted to be intrinsically disordered. Hence, a monomer of L-PRX, assumed to be mainly in random coil conformation, could reach a length of >30 nm (Fitzkee and Rose, 2004), which would be nearly doubled in the case of an L-PRX dimer formed through domain swapping at the N-terminal PDZ-like domain (Han and Kursula, 2014). PRX may thus be able to act as a molecular ruler and mediate protein interactions across partners distributed widely across the Schwann cell abaxonal membrane. The distance between bound DRP2 and β4 integrin can be estimated to be up to ∼25–30 nm, depending on the exact binding site and the conformation of L-PRX between the binding sites. The flexibility of L-PRX should allow it to stay bound to both protein complexes, even in the case they rearrange on the membrane. Such interactions might be possible, for example, at the edges between abaxonal membrane appositions and Cajal bands.

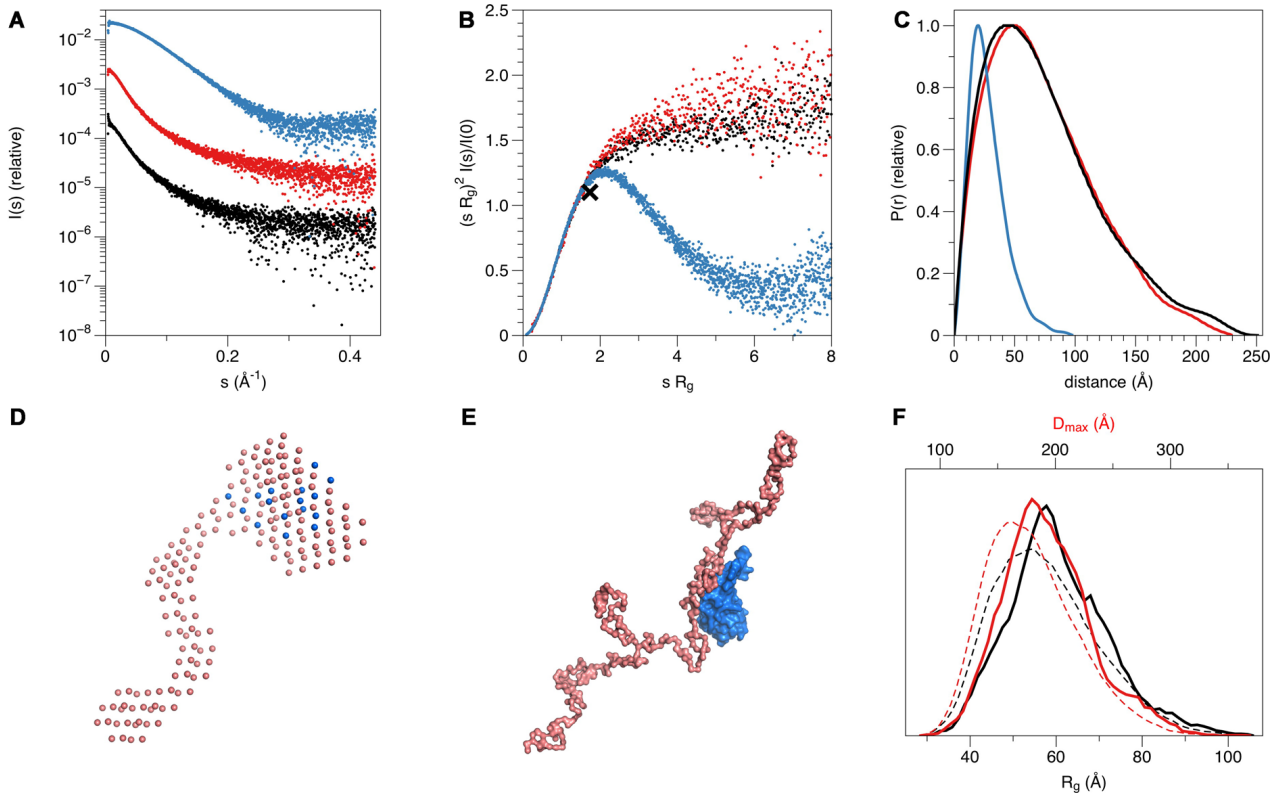

FIGURE 5 | Structure of the complex in solution. **(A)** Small-angle X-ray scattering (SAXS) scattering curve. PRX-C, red; β4-FNIII-3, blue; complex, black. **(B)** Dimensionless Kratky plot. The black cross indicates the theoretical peak position for a folded, perfectly globular protein. **(C)** Distance distribution function. **(D)** Multi-phase model from MONSA. PRX-C, pink; β4-FNIII-3, blue. **(E)** Rigid-body fit between a chain-like model of PRX-C (pink) and the integrin crystal structure (blue). **(F)** EOM analysis for PRX-C. Dashed lines, theoretical distribution for a random coil; solid lines, the ensemble for PRX-C. Maximum dimension is shown in red and radius of gyration in black. PRX-C is slightly more elongated than a random coil.

Insights From Structure of the Protein Complex

The binding site for β4 integrin in L-PRX remains unknown, although the mapping in this study suggests that the acidic region of L-PRX is involved. A sequence alignment of this region (**Figure 3B**) from different species shows that only a few segments are highly conserved; it is conceivable that these regions have functional relevance and they could form the binding site. Further studies will be required to obtain higher-resolution structural data to fully understand the binding interactions.

Typical modes of target protein binding by FNIII domains include transient opening and domain swapping (Ohashi et al., 2009). It is possible that some of the conserved segments in L-PRX are involved in a domain-swapping rearrangement of β4-FNIII-3. Such a mechanism would be compatible with the lack of change in secondary structure content upon complex formation, which we observed in SRCD experiments. High-resolution structural studies should answer many of the currently open questions, which will require the identification of the exact binding site(s).

Considering the structures of both L-PRX and β4 integrin, it is possible that additional binding surfaces are present in both proteins. β4 integrin has four FNIII domains in its cytoplasmic domain, and the C-terminal region of L-PRX is large and flexible, containing repetitive sequences. The fourth FNIII domain of β4 integrin does not bind to PRX-C (**Supplementary Figure S1**), however, and it is important to recapitulate that the stoichiometry of the interaction between PRX-C and β4-FNIII-3 was observed here to be 1:1.

Relevance for Understanding Demyelinating Disease

A number of proteins have been characterized as targets for mutations in human hereditary neuropathies, whereby the structure of the myelin sheath is compromised. Detailed knowledge about protein interactions in myelin is required to accurately understand the molecular bases of such diseases. One such protein is PRX, which is expressed as two isoforms, S- and L-PRX. While S-PRX consists of only a dimeric PDZ-like domain and a short tail, L-PRX dimerizes through the N terminus similarly to S-PRX (Han and Kursula, 2014), but has in total ∼1,400 residues. Little is known about the structure and function of the long, repetitive L-PRX-specific segments. Expression of S-PRX may result in PRX heterodimerization (Yang and Shi, 2015) and affect the regulation of the PRX-containing protein scaffold, as S-PRX interacts with neither DRP2 nor β4 integrin.

Most PRX mutations causing human hereditary neuropathy introduce a premature stop codon into the sequence (Guilbot et al., 2001; Tokunaga et al., 2012; Choi et al., 2015). In line with this, patients with such mutations have PRX expressed, but its size is smaller than in normal individuals (Parman et al., 2004; Kabzinska et al., 2006). These observations hint at the possibility that an important function of L-PRX during myelin formation and maintenance lies at its C-terminal region. This is intriguing, given our observation that this region of L-PRX is intrinsically disordered. Here, we have shown a tight interaction between this C-terminal region and the third FNIII domain in the β4 integrin cytoplasmic domain—in the case of PRX truncations, such an interaction would be abolished. This would be expected to cause large-scale disturbances in the PRX-related protein scaffold reaching to the basal lamina and may translate to defects in myelin maintenance, such as the loss of membrane appositions in the ΔCPrxTg/Prx$^{-/-}$ mice (Sherman and Brophy, 2018). Interactions with DRP2 are important for PRX function, but for a stable myelin sheath, links between the Schwann cell cytoplasm and the basal lamina through β4 integrin may be crucial. L-PRX, hence, mediates a two-pronged interaction from the cytoplasmic side through the Schwann cell plasma membrane to the basal lamina (**Figure 7**) and might have a role in sequestering different types of laminin receptors. How this relates to the formation and stability of appositions and Cajal bands *in vivo* still remains to be determined. The identification of β4 integrin as another L-PRX ligand provides an important starting point for future studies.

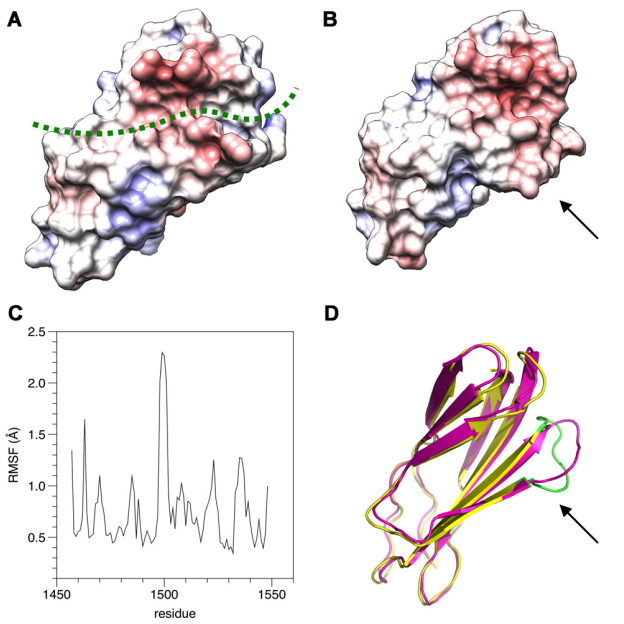

FIGURE 6 | Possible binding site for L-PRX. **(A)** Surface of the β4-FNIII-3 crystal structure, colored by electrostatic potential. The predicted binding site is shown by a green dashed line. **(B)** MD simulation indicates the possible binding site is flexible (arrow) and may open up more. **(C)** RMSF during the 550-ns simulation. **(D)** Comparison of the start (magenta) and end (yellow/green) points of the simulation. The loop at the potential binding site (arrow) is the most mobile region. The largest peak in the RMSF plot (panel **C**) is colored green in the post-simulation structure.

Loss of O-glycosylation causes similar phenotypic effects as L-PRX truncation in mouse models of CMT4F (Kim et al., 2016). Several O-glycosylation sites in PRX were identified, and some of them reside in the C-terminal region, which binds to β4 integrin. It is possible that PTMs, including O-glycosylation, regulate PRX interactions with β4 integrin in a dynamic manner.

Integrin β4 has been highlighted both as a biomarker for Guillain-Barré syndrome (Sessa et al., 1997; Previtali et al., 1998; Archelos et al., 1999), an autoimmune demyelinating disease of peripheral nerves, and as a central molecule in the entry of *Mycobacterium leprae* into Schwann cells, *via* the basal lamina (Rambukkana et al., 1997). Leprosy is characterized by peripheral nerve damage initiated by mycobacterial infection of

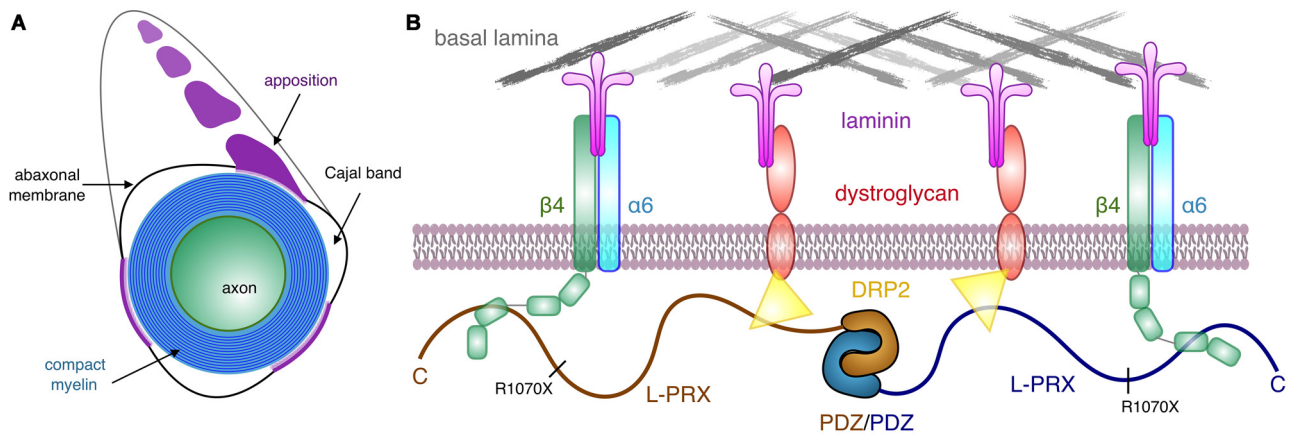

FIGURE 7 | Schematic view of the PRX-linked protein scaffold in peripheral nervous system (PNS) myelin. **(A)** Cross section of a myelinated peripheral axon, showing compact myelin, the abaxonal membrane, Cajal bands, and appositions. While dystrophin-related protein 2 (DRP2) is restricted to the appositions, and PRX is concentrated in them, β4 integrin is involved in signaling in the Cajal bands (Salzer, 2015). **(B)** A possible architecture for L-PRX-based protein scaffolds at the Schwann cell abaxonal membrane. The position of the truncating R1070X mutation in L-PRX is indicated, and the β4 integrin binding site lies C-terminal to it, although an exact binding site remains to be identified.

the Schwann cells. It is currently not known, how L-PRX binding to β4 integrin might modulate this process. Our data provide starting points for such studies in the future.

CONCLUSION

The dimeric, highly elongated, flexible L-PRX is capable of acting as a central protein scaffold within non-compact myelin, linking integrins and dystroglycans together, thus bridging together two major protein complexes linking Schwann cells to the extracellular matrix. This could have high relevance in ensuring the formation and necessary stability of membrane appositions that drive the formation of Cajal bands. The PRX-β4 integrin complex is likely to be important in both normal myelination, myelin maintenance, as well as the pathophysiology of neurodegenerative disease. Obviously, additional *in vivo* and structural biology approaches will be required in the future to fully corroborate our data and relate them to myelin development and the demyelinating phenotype in CMT4F.

ETHICS STATEMENT

Experiments conducted during the course of this study received approval from the University of Edinburgh's Local Ethical Review Board. Animal breeding and maintenance and experimental procedures were performed in accordance with the UK Animals (Scientific Procedures) Act 1986 under the authority of Project Licence P0F4A25E9 (PB).

AUTHOR CONTRIBUTIONS

PB, DS, and PK conceived the project. DS and PB carried out and analyzed yeast two-hybrid, immunochemical, and proteomics experiments. AR and HL performed experiments with purified proteins. AR and PK performed analysis of protein structure. AR, DS, and PK drafted the manuscript. All authors contributed to manuscript revision.

FUNDING

This work was financially supported by the Norwegian Research Council (Norges Forskningsråd) travel grant to PK (SYNKNØYT 247669), as well as a Wellcome Trust (107008/Z/15/Z) grant to PB.

ACKNOWLEDGMENTS

We gratefully acknowledge the synchrotron radiation facilities and the beamline support at ASTRID2, DLS, ESRF, and EMBL/DESY. We express our gratitude towards the Biocenter Oulu Proteomics and Protein Analysis Core Facility and Dr Ulrich Bergmann for providing access to mass spectrometric instrumentation, as well as Biophysics, Structural Biology, and Screening (BiSS) facilities at University of Bergen for providing calorimetric equipment and crystallization facilities. We thank Lisa Imrie for performing mass spectrometry and Qiushi Li for assistance. We are grateful to NanoTemper Technologies GmbH and Dr Teresia Hallström for providing access to nanoDSF instrumentation. This manuscript has been released as a pre-print at bioRxiv (Raasakka et al., 2019b).

SUPPLEMENTARY MATERIAL

The Supplementary Material for this article can be found online at: https://www.frontiersin.org/articles/10.3389/fnmol.2019.00084/full#supplementary-material

REFERENCES

Afonine, P. V., Grosse-Kunstleve, R. W., Echols, N., Headd, J. J., Moriarty, N. W., Mustyakimov, M., et al. (2012). Towards automated crystallographic structure refinement with phenix.refine. *Acta Crystallogr. D Biol. Crystallogr.* 68, 352–367. doi: 10.1107/S0907444912001308

Alonso-García, N., García-Rubio, I., Manso, J. A., Buey, R. M., Urien, H., Sonnenberg, A., et al. (2015). Combination of X-ray crystallography, SAXS and DEER to obtain the structure of the FnIII-3,4 domains of integrin a6ß4. *Acta Crystallogr. D Biol. Crystallogr.* 71, 969–985. doi: 10.1107/s1399004715002485

Archelos, J. J., Previtali, S. C., and Hartung, H. P. (1999). The role of integrins in immune-mediated diseases of the nervous system. *Trends Neurosci* 22, 30–38. doi: 10.1016/s0166-2236(98)01287-9

Barbar, E., and Nyarko, A. (2015). Polybivalency and disordered proteins in ordering macromolecular assemblies. *Semin. Cell Dev. Biol.* 37, 20–25. doi: 10.1016/j.semcdb.2014.09.016

Bernadó, P., and Blackledge, M. (2009). A self-consistent description of the conformational behavior of chemically denatured proteins from NMR and small angle scattering. *Biophys. J.* 97, 2839–2845. doi: 10.1016/j.bpj.2009.08.044

Bernadó, P., Mylonas, E., Petoukhov, M. V., Blackledge, M., and Svergun, D. I. (2007). Structural characterization of flexible proteins using small-angle X-ray scattering. *J. Am. Chem. Soc.* 129, 5656–5664. doi: 10.1021/ja069124n

Boerkoel, C. F., Takashima, H., Garcia, C. A., Olney, R. K., Johnson, J., Berry, K., et al. (2002). Charcot-Marie-Tooth disease and related neuropathies: mutation distribution and genotype-phenotype correlation. *Ann. Neurol.* 51, 190–201. doi: 10.1002/ana.10089

Bowler, M. W., Nurizzo, D., Barrett, R., Beteva, A., Bodin, M., Caserotto, H., et al. (2015). MASSIF-1: a beamline dedicated to the fully automatic characterization and data collection from crystals of biological macromolecules. *J. Synchrotron Radiat.* 22, 1540–1547. doi: 10.1107/s1600577515016604

Brennan, K. M., Bai, Y., Pisciotta, C., Wang, S., Feely, S. M., Hoegger, M., et al. (2015). Absence of dystrophin related protein-2 disrupts cajal bands in a patient with charcot-marie-tooth disease. *Neuromuscul. Disord.* 25, 786–793. doi: 10.1016/j.nmd.2015.07.001

Calmettes, P., Durand, D., Desmadril, M., Minard, P., Receveur, V., and Smith, J. C. (1994). How random is a highly denatured protein. *Biophys. Chem.* 53, 105–113. doi: 10.1016/0301-4622(94)00081-6

Choi, Y. J., Hyun, Y. S., Nam, S. H., Koo, H., Hong, Y. B., Chung, K. W., et al. (2015). Novel compound heterozygous nonsense PRX mutations in a korean dejerine-sottas neuropathy family. *J. Clin. Neurol.* 11, 92–96. doi: 10.3988/jcn.2015.11.1.92

Cianci, M., Bourenkov, G., Pompidor, G., Karpics, I., Kallio, J., Bento, I., et al. (2017). P13, the EMBL macromolecular crystallography beamline at the low-emittance PETRA III ring for high- and low-energy phasing with variable beam focusing. *J. Synchrotron Radiat.* 24, 323–332. doi: 10.1107/s1600577516016465

Court, F. A., Sherman, D. L., Pratt, T., Garry, E. M., Ribchester, R. R., Cottrell, D. F., et al. (2004). Restricted growth of Schwann cells lacking Cajal bands slows conduction in myelinated nerves. *Nature* 431, 191–195. doi: 10.1038/nature02841

Davis, I. W., Murray, L. W., Richardson, J. S., and Richardson, D. C. (2004). MOLPROBITY: structure validation and all-atom contact analysis

for nucleic acids and their complexes. *Nucleic Acids Res.* 32, W615–W619. doi: 10.1093/nar/gkh398

de Monasterio-Schrader, P., Jahn, O., Tenzer, S., Wichert, S. P., Patzig, J., and Werner, H. B. (2012). Systematic approaches to central nervous system myelin. *Cell. Mol. Life Sci.* 69, 2879–2894. doi: 10.1007/s00018-012-0958-9

DiVincenzo, C., Elzinga, C. D., Medeiros, A. C., Karbassi, I., Jones, J. R., Evans, M. C., et al. (2014). The allelic spectrum of Charcot-Marie-Tooth disease in over 17,000 individuals with neuropathy. *Mol. Genet. Genomic Med.* 2, 522–529. doi: 10.1002/mgg3.106

Dolinsky, T. J., Nielsen, J. E., McCammon, J. A., and Baker, N. A. (2004). PDB2PQR: an automated pipeline for the setup of Poisson-Boltzmann electrostatics calculations. *Nucleic Acids Res.* 32, W665–W667. doi: 10.1093/nar/gkh381

Drozdetskiy, A., Cole, C., Procter, J., and Barton, G. J. (2015). JPred4: a protein secondary structure prediction server. *Nucleic Acids Res.* 43, W389–W394. doi: 10.1093/nar/gkv332

Dytrych, L., Sherman, D. L., Gillespie, C. S., and Brophy, P. J. (1998). Two PDZ domain proteins encoded by the murine periaxin gene are the result of alternative intron retention and are differentially targeted in Schwann cells. *J. Biol. Chem.* 273, 5794–5800. doi: 10.1074/jbc.273.10.5794

Einheber, S., Milner, T. A., Giancotti, F., and Salzer, J. L. (1993). Axonal regulation of Schwann cell integrin expression suggests a role for α 6 β 4 in myelination. *J. Cell Biol.* 123, 1223–1236. doi: 10.1083/jcb.123.5.1223

Emsley, P., Lohkamp, B., Scott, W. G., and Cowtan, K. (2010). Features and development of Coot. *Acta Crystallogr. D Biol. Crystallogr.* 66, 486–501. doi: 10.1107/S0907444910007493

Feltri, M. L., Graus Porta, D., Previtali, S. C., Nodari, A., Migliavacca, B., Cassetti, A., et al. (2002). Conditional disruption of β 1 integrin in Schwann cells impedes interactions with axons. *J. Cell Biol.* 156, 199–209. doi: 10.1083/jcb.200109021

Feltri, M. L., Scherer, S. S., Nemni, R., Kamholz, J., Vogelbacker, H., Scott, M. O., et al. (1994). β 4 integrin expression in myelinating Schwann cells is polarized, developmentally regulated and axonally dependent. *Development* 120, 1287–1301.

Fitzkee, N. C., and Rose, G. D. (2004). Reassessing random-coil statistics in unfolded proteins. *Proc. Natl. Acad. Sci. U S A* 101, 12497–12502. doi: 10.1073/pnas.0404236101

Gillespie, C. S., Sherman, D. L., Blair, G. E., and Brophy, P. J. (1994). Periaxin, a novel protein of myelinating Schwann cells with a possible role in axonal ensheathment. *Neuron* 12, 497–508. doi: 10.1016/0896-6273(94)90208-9

Gillespie, C. S., Sherman, D. L., Fleetwood-Walker, S. M., Cottrell, D. F., Tait, S., Garry, E. M., et al. (2000). Peripheral demyelination and neuropathic pain behavior in periaxin-deficient mice. *Neuron* 26, 523–531. doi: 10.1016/s0896-6273(00)81184-8

Guilbot, A., Williams, A., Ravisé, N., Verny, C., Brice, A., Sherman, D. L., et al. (2001). A mutation in periaxin is responsible for CMT4F, an autosomal recessive form of Charcot-Marie-Tooth disease. *Hum. Mol. Genet.* 10, 415–421. doi: 10.1093/hmg/10.4.415

Han, H., and Kursula, P. (2014). Periaxin and AHNAK nucleoprotein 2 form intertwined homodimers through domain swapping. *J. Biol. Chem.* 289, 14121–14131. doi: 10.1074/jbc.m114.554816

Han, H., Myllykoski, M., Ruskamo, S., Wang, C., and Kursula, P. (2013). Myelin-specific proteins: a structurally diverse group of membrane-interacting molecules. *Biofactors* 39, 233–241. doi: 10.1002/biof.1076

Harauz, G., Ladizhansky, V., and Boggs, J. M. (2009). Structural polymorphism and multifunctionality of myelin basic protein. *Biochemistry* 48, 8094–8104. doi: 10.1021/bi901005f

Hartline, D. K. (2008). What is myelin. *Neuron Glia Biol.* 4, 153–163. doi: 10.1017/S1740925X09990263

Jie, J., Löhr, F., and Barbar, E. (2015). interactions of yeast dynein with dynein light chain and dynactin: general implications for intrinsically disordered duplex scaffolds in multiprotein assemblies. *J. Biol. Chem.* 290, 23863–23874. doi: 10.1074/jbc.m115.649715

Johnson, W. C. (1999). Analyzing protein circular dichroism spectra for accurate secondary structures. *Proteins* 35, 307–312. doi: 10.1002/(sici)1097-0134(19990515)35:3<307::aid-prot4 >3.0.co;2-3

Jurrus, E., Engel, D., Star, K., Monson, K., Brandi, J., Felberg, L. E., et al. (2018). Improvements to the APBS biomolecular solvation software suite. *Protein Sci.* 27, 112–128. doi: 10.1002/pro.3280

Kabsch, W. (2010). XDS. *Acta Crystallogr. D Biol. Crystallogr.* 66, 125–132. doi: 10.1107/S0907444909047337

Kabsch, W., and Sander, C. (1983). Dictionary of protein secondary structure: pattern recognition of hydrogen-bonded and geometrical features. *Biopolymers* 22, 2577–2637. doi: 10.1002/bip.360221211

Kabzinska, D., Drac, H., Sherman, D. L., Kostera-Pruszczyk, A., Brophy, P. J., Kochanski, A., et al. (2006). Charcot-Marie-Tooth type 4F disease caused by S399fsx410 mutation in the PRX gene. *Neurology* 66, 745–747. doi: 10.1212/01.wnl.0000201269.46071.35

Kim, S., Maynard, J. C., Sasaki, Y., Strickland, A., Sherman, D. L., Brophy, P. J., et al. (2016). Schwann cell O-GlcNAc glycosylation is required for myelin maintenance and axon integrity. *J. Neurosci.* 36, 9633–9646. doi: 10.1523/JNEUROSCI.1235-16.2016

Krieger, E., and Vriend, G. (2015). New ways to boost molecular dynamics simulations. *J. Comput. Chem.* 36, 996–1007. doi: 10.1002/jcc.23899

Lees, J. G., Miles, A. J., Wien, F., and Wallace, B. A. (2006). A reference database for circular dichroism spectroscopy covering fold and secondary structure space. *Bioinformatics* 22, 1955–1962. doi: 10.1093/bioinformatics/btl327

Luo, X., Sharma, D., Inouye, H., Lee, D., Avila, R. L., Salmona, M., et al. (2007). Cytoplasmic domain of human myelin protein zero likely folded as β-structure in compact myelin. *Biophys. J.* 92, 1585–1597. doi: 10.1529/biophysj.106.094722

Masaki, T., Matsumura, K., Hirata, A., Yamada, H., Hase, A., Arai, K., et al. (2002). Expression of dystroglycan and the laminin-α 2 chain in the rat peripheral nerve during development. *Exp. Neurol.* 174, 109–117. doi: 10.1006/exnr.2001.7856

McCoy, A. J., Grosse-Kunstleve, R. W., Adams, P. D., Winn, M. D., Storoni, L. C., and Read, R. J. (2007). Phaser crystallographic software. *J. Appl. Crystallogr.* 40, 658–674. doi: 10.1107/S0021889807021206

Micsonai, A., Wien, F., Bulyáki, É., Kun, J., Moussong, É., Lee, Y. H., et al. (2018). BeStSel: a web server for accurate protein secondary structure prediction and fold recognition from the circular dichroism spectra. *Nucleic Acids Res.* 46, W315–W322. doi: 10.1093/nar/gky497

Mittendorf, K. F., Kroncke, B. M., Meiler, J., and Sanders, C. R. (2014). The homology model of PMP22 suggests mutations resulting in peripheral neuropathy disrupt transmembrane helix packing. *Biochemistry* 53, 6139–6141. doi: 10.1021/bi500809t

Myllykoski, M., Eichel, M. A., Jung, R. B., Kelm, S., Werner, H. B., and Kursula, P. (2018). High-affinity heterotetramer formation between the large myelin-associated glycoprotein and the dynein light chain DYNLL1. *J. Neurochem.* 147, 764–783. doi: 10.1111/jnc.14598

Nave, K. A. (2010). Myelination and the trophic support of long axons. *Nat. Rev. Neurosci.* 11, 275–283. doi: 10.1038/nrn2797

Nodari, A., Previtali, S. C., Dati, G., Occhi, S., Court, F. A., Colombelli, C., et al. (2008). α6β4 integrin and dystroglycan cooperate to stabilize the myelin sheath. *J. Neurosci.* 28, 6714–6719. doi: 10.1523/JNEUROSCI.0326-08.2008

Ohashi, T., Augustus, A. M., and Erickson, H. P. (2009). Transient opening of fibronectin type III (FNIII) domains: the interaction of the third FNIII domain of FN with anastellin. *Biochemistry* 48, 4189–4197. doi: 10.1021/bi900001g

Otagiri, T., Sugai, K., Kijima, K., Arai, H., Sawaishi, Y., Shimohata, M., et al. (2006). Periaxin mutation in Japanese patients with Charcot-Marie-Tooth disease. *J. Hum. Genet.* 51, 625–628. doi: 10.1007/s10038-006-0408-3

Parman, Y., Battaloglu, E., Baris, I., Bilir, B., Poyraz, M., Bissar-Tadmouri, N., et al. (2004). Clinicopathological and genetic study of early-onset demyelinating neuropathy. *Brain* 127, 2540–2550. doi: 10.1093/brain/awh275

Petoukhov, M. V., Franke, D., Shkumatov, A. V., Tria, G., Kikhney, A. G., Gajda, M., et al. (2012). New developments in the ATSAS program package for small-angle scattering data analysis. *J. Appl. Crystallogr.* 45, 342–350. doi: 10.1107/S0021889812007662

Petoukhov, M. V., and Svergun, D. I. (2005). Global rigid body modelling of macromolecular complexes against small-angle scattering data. *Biophys. J.* 89, 1237–1250.

Pettersen, E. F., Goddard, T. D., Huang, C. C., Couch, G. S., Greenblatt, D. M., Meng, E. C., et al. (2004). UCSF Chimera—a visualization system for

exploratory research and analysis. *J. Comput. Chem.* 25, 1605–1612. doi: 10.1002/jcc.20084

Poitelon, Y., Lopez-Anido, C., Catignas, K., Berti, C., Palmisano, M., Williamson, C., et al. (2016). YAP and TAZ control peripheral myelination and the expression of laminin receptors in Schwann cells. *Nat. Neurosci.* 19, 879–887. doi: 10.1038/nn.4316

Poitelon, Y., Matafora, V., Silvestri, N., Zambroni, D., McGarry, C., Serghany, N., et al. (2018). A dual role for Integrin a6ß4 in modulating hereditary neuropathy with liability to pressure palsies. *J. Neurochem.* 145, 245–257. doi: 10.1111/jnc.14295

Ponna, S. K., Myllykoski, M., Boeckers, T. M., and Kursula, P. (2017). Structure of an unconventional SH3 domain from the postsynaptic density protein Shank3 at ultrahigh resolution. *Biochem. Biophys. Res. Commun.* 490, 806–812. doi: 10.1016/j.bbrc.2017.06.121

Previtali, S. C., Archelos, J. J., and Hartung, H. P. (1998). Expression of integrins in experimental autoimmune neuritis and Guillain-Barré syndrome. *Ann. Neurol.* 44, 611–621. doi: 10.1002/ana.410440406

Raasakka, A., Ruskamo, S., Kowal, J., Han, H., Baumann, A., Myllykoski, M., et al. (2019a). Molecular structure and function of myelin protein P0 in membrane stacking. *Sci. Rep.* 9:642. doi: 10.1038/s41598-018-37009-4

Raasakka, A., Linxweiler, H., Brophy, P. J., Sherman, D. L., and Kursula, P. (2019b). Direct binding of the flexible C-terminal segment of periaxin to ß4 integrin suggests a molecular basis for CMT4F. *bioRxiv* [Preprint]. 524793. doi: 10.1101/524793

Raasakka, A., Ruskamo, S., Kowal, J., Barker, R., Baumann, A., Martel, A., et al. (2017). Membrane association landscape of myelin basic protein portrays formation of the myelin major dense line. *Sci. Rep.* 7:4974. doi: 10.1038/s41598-017-05364-3

Rambukkana, A., Salzer, J. L., Yurchenco, P. D., and Tuomanen, E. I. (1997). Neural targeting of *Mycobacterium leprae* mediated by the G domain of the laminin-α2 chain. *Cell* 88, 811–821. doi: 10.1016/s0092-8674(00)81927-3

Ruskamo, S., Nieminen, T., Kristiansen, C. K., Vatne, G. H., Baumann, A., Hallin, E. I., et al. (2017). Molecular mechanisms of Charcot-Marie-Tooth neuropathy linked to mutations in human myelin protein P2. *Sci. Rep.* 7:6510. doi: 10.1038/s41598-017-06781-0

Sakakura, M., Hadziselimovic, A., Wang, Z., Schey, K. L., and Sanders, C. R. (2011). Structural basis for the Trembler-J phenotype of Charcot-Marie-Tooth disease. *Structure* 19, 1160–1169. doi: 10.1016/j.str.2011.05.009

Salzer, J. L. (2015). Schwann cell myelination. *Cold Spring Harb. Perspect. Biol.* 7:a020529. doi: 10.1101/cshperspect.a020529

Scherer, S. S., Xu, Y. T., Bannerman, P. G., Sherman, D. L., and Brophy, P. J. (1995). Periaxin expression in myelinating Schwann cells: modulation by axon-glial interactions and polarized localization during development. *Development* 121, 4265–4273.

Sessa, G., Nemni, R., Canal, N., and Marchisio, P. C. (1997). Circulating fragments of myelin-associated α 6 β 4 integrin in Guillain-Barré syndrome. *J. Neuroimmunol.* 80, 115–120. doi: 10.1016/s0165-5728(97)00143-4

Sherman, D. L., and Brophy, P. J. (2000). A tripartite nuclear localization signal in the PDZ-domain protein L-periaxin. *J. Biol. Chem.* 275, 4537–4540. doi: 10.1074/jbc.275.7.4537

Sherman, D. L., and Brophy, P. J. (2005). Mechanisms of axon ensheathment and myelin growth. *Nat. Rev. Neurosci.* 6, 683–690. doi: 10.1038/nrn1743

Sherman, D. L., and Brophy, P. J. (2018). A murine model of Charcot-Marie-Tooth disease 4F reveals a role for the C-terminus of periaxin in the formation and stabilization of Cajal bands. *Wellcome Open Res.* 3:20. doi: 10.12688/wellcomeopenres.13673.1

Sherman, D. L., Fabrizi, C., Gillespie, C. S., and Brophy, P. J. (2001). Specific disruption of a schwann cell dystrophin-related protein complex in a demyelinating neuropathy. *Neuron* 30, 677–687. doi: 10.1016/s0896-6273(01)00327-0

Sherman, D. L., Wu, L. M., Grove, M., Gillespie, C. S., and Brophy, P. J. (2012). Drp2 and periaxin form Cajal bands with dystroglycan but have distinct roles in Schwann cell growth. *J. Neurosci.* 32, 9419–9428. doi: 10.1523/JNEUROSCI.1220-12.2012

Snaidero, N., Velte, C., Myllykoski, M., Raasakka, A., Ignatev, A., Werner, H. B., et al. (2017). Antagonistic functions of MBP and CNP establish cytosolic channels in CNS myelin. *Cell Rep.* 18, 314–323. doi: 10.1016/j.celrep.2016.12.053

Svensson, O., Malbet-Monaco, S., Popov, A., Nurizzo, D., and Bowler, M. W. (2015). Fully automatic characterization and data collection from crystals of biological macromolecules. *Acta Crystallogr. D Biol. Crystallogr.* 71, 1757–1767. doi: 10.1107/s1399004715011918

Svergun, D. I. (1992). Determination of the regularization parameter in indirect-transform methods using perceptual criteria. *J. Appl. Cryst.* 25, 495–503. doi: 10.1107/s0021889892001663

Svergun, D. I. (1999). Restoring low resolution structure of biological macromolecules from solution scattering using simulated annealing. *Biophys. J.* 76, 2879–2886. doi: 10.1016/s0006-3495(99)77443-6

Svergun, D. I., Petoukhov, M. V., and Koch, M. H. (2001). Determination of domain structure of proteins from X-ray solution scattering. *Biophys. J.* 80, 2946–2953. doi: 10.1016/s0006-3495(01)76260-1

Takashima, H., Boerkoel, C. F., De Jonghe, P., Ceuterick, C., Martin, J. J., Voit, T., et al. (2002). Periaxin mutations cause a broad spectrum of demyelinating neuropathies. *Ann. Neurol.* 51, 709–715. doi: 10.1002/ana.10213

Tokunaga, S., Hashiguchi, A., Yoshimura, A., Maeda, K., Suzuki, T., Haruki, H., et al. (2012). Late-onset Charcot-Marie-Tooth disease 4F caused by periaxin gene mutation. *Neurogenetics* 13, 359–365. doi: 10.1007/s10048-012-0338-5

Ushiki, T., and Ide, C. (1987). Scanning electron microscopic studies of the myelinated nerve fibres of the mouse sciatic nerve with special reference to the Schwann cell cytoplasmic network external to the myelin sheath. *J. Neurocytol.* 16, 737–747. doi: 10.1007/bf01611982

van den Berg, S., Löfdahl, P. A., Härd, T., and Berglund, H. (2006). Improved solubility of TEV protease by directed evolution. *J. Biotechnol.* 121, 291–298. doi: 10.1016/j.jbiotec.2005.08.006

Whitmore, L., and Wallace, B. A. (2004). DICHROWEB, an online server for protein secondary structure analyses from circular dichroism spectroscopic data. *Nucleic Acids Res.* 32, W668–W673. doi: 10.1093/nar/gkh371

Wu, L. M., Williams, A., Delaney, A., Sherman, D. L., and Brophy, P. J. (2012). Increasing internodal distance in myelinated nerves accelerates nerve conduction to a flat maximum. *Curr. Biol.* 22, 1957–1961. doi: 10.1016/j.cub.2012.08.025

Xie, L., and Bourne, P. E. (2005). Functional coverage of the human genome by existing structures, structural genomics targets, and homology models. *PLoS Comput. Biol.* 1:e31. doi: 10.1371/journal.pcbi.0010031

Yang, Y., and Shi, Y. (2015). L-periaxin interacts with S-periaxin through its PDZ domain. *Neurosci. Lett.* 609, 23–29. doi: 10.1016/j.neulet.2015.10.020

Conflict of Interest Statement: The authors declare that the research was conducted in the absence of any commercial or financial relationships that could be construed as a potential conflict of interest.